ELSEVIER

Contents lists available at ScienceDirect

Journal of the European Ceramic Society

journal homepage: www.elsevier.com/locate/jeurceramsoc





Applying archaeomagnetic methods to virtually reconstruct medieval pavements: Insights from Tiebas Castle (Spain)

Iván Ruiz-Ardanaz a,b,*, Esther Lasheras a,b, Adrián Durán a,b,*,

- a BIOMA Institute for Biodiversity and Environment, University of Navarra, Irunlarrea 1, Pamplona 31008, Spain
- ^b School of Science, Chemistry Department, University of Navarra, Irunlarrea 1, Pamplona 31008, Spain

ARTICLE INFO

Keywords:
Archaeomagnetism
Carreaux de pavement
Magnetic minerals
Mediaeval ceramics

ABSTRACT

Archaeomagnetic dating is commonly applied to baked clay materials. Through these methods, the chronology is calculated by analysing the material's remanent magnetism and knowing its original position. Here, the reverse approach was applied: knowing the chronology and remaining magnetism, the original orientation was virtually reconstructed. This reverse method was tested on some tiles from Tiebas Castle (Spain) proving novel insights of its pavements. The object of analysis was a set of tiles that had been heated twice: first during their manufacture in the mid-13th century, and after, during the castle destruction by a fire in 1378, when they were part of the pavement. Through these results it was determined which halls were covered with tiles and to estimate their original orientation in them. Additionally, it has been possible to estimate the temperatures reached during the fire (240–540 °C). This novel application demonstrates potential for broader use in reconstructing archaeological ceramic structures like kilns, ovens, or pottery.

1. Introduction

1.1. Pottery magnetic minerals

In pottery pastes, most of the matter is diamagnetic, such as quartz or calcite; or paramagnetic, like most philosophicates [1-3]. However, they often contain amounts of ferromagnetic minerals, such as iron oxides, iron hydroxides that have remanent magnetization [3,4]. The most frequent ferromagnetic minerals found in natural clay, which can also be found in ceramic pastes, are haematite (α-Fe₂O₃), magnetite (Fe₃O₄), maghemite (γ-Fe₂O₃), goethite (α-FeO-OH), the series of solid solutions of iron and titanium oxides (ilmenite-FeTiO3 and ulvospinel-Fe₂TiO₄) [3,4]. In ceramic pastes, these magnetic minerals could come from the raw clay or have been produced during firing from the decomposition of iron hydroxides, such as goethite and lepidocrocite; or Fe-bearing clays, such as phyllosilicates [5]. Haematite and goethite are antiferromagnetic and have χ_m of $60\cdot10^{-8}$ m 3 Kg $^{-1}$ and $70\cdot10^{-8}$ m 3 Kg $^{-1}$ respectively [1,5]. Magnetite and maghemite are ferrimagnetic and have χ_m of $50000 \cdot 10^{-8}$ m³Kg⁻¹ and $40000 \cdot 10^{-8}$ m³Kg⁻¹ [1,5]. In the case of titanohaematite ($Ti_xFe_{2-x}O_3$, $0 \le x \le 1$), it is antiferromagnetic and its χ_m usually drops until values ca. $200 \cdot 10^{-8} \text{ m}^3 \text{Kg}^{-1}$ for ilmenite (FeTiO₃) which is paramagnetic at ambient temperature [1,5].

Clay materials, composed of small grains, have net remanent magnetism depending on the ordering of these grains, but is usually negligible since the magnetic moments of the grains are generally arranged randomly. Materials composed of several grains or domains can acquire or modify the orientation of their overall magnetism through the process of Remanent Magnetization (RM). The RM of a material is the process in which its ferromagnetic, ferrimagnetic or antiferromagnetic components orientate some of their magnetic domains towards the same preferred direction and sense. This process can frequently occur by heating-cooling processes, also known as Thermal Remanent Magnetization (TRM); chemical reactions, known as Chemical Remanent Magnetization (CRM); or sedimentation, known as Detrital Remanent Magnetization (DRM) [3].

The clay used as raw material in pottery production may have DRM or CRM due to previous sedimentation processes, where the magnetic domains were ordered preferentially to the Earth Magnetic Field (EMF) direction and sense. However, this RM is lost during wet clay modelling as the magnetic domains are moved and mixed so their orientations are messed up randomly, obtaining a null global magnetism. Later on, after kiln firing, the domains can acquire a TRM. When ferrimagnetic or

DOI of original article: https://doi.org/10.1016/j.jeurceramsoc.2025.117343.

^{*} Corresponding authors at: BIOMA Institute for Biodiversity and Environment, University of Navarra, Irunlarrea 1, Pamplona 31008, Spain. *E-mail addresses*: iruiz.23@alumni.unav.es (I. Ruiz-Ardanaz), adrianduran@unav.es (A. Durán).

antiferromagnetic materials are heated above a determined temperature their magnetic domains become randomly ordered (paramagnetism). This transition temperature to a paramagnetic state is called Curie temperature (T_C) for ferromagnetic and ferrimagnetic minerals, and Neel temperature (T_N) for antiferromagnetic minerals. However, as they cool down, they preferentially acquire the direction of the external magnetic field (generally the Earth's Magnetic Field (EMF)). For these reasons, the magnetization intensity of the ceramics depends on their magnetic mineral abundance, the magnetic properties of the minerals, the cooling rate, the size of the ferromagnetic grains, anisotropy and the intensity of the EMF. Haematite and goethite have T_{N} of 675 °C and 120 °C, respectively [4,6]. Magnetite and maghemite have T_C of 580 °C and 640 °C, respectively [4,6]. In the case of titanomagnetite (Ti_xFe_{3-x}O₄, $0 \le x \le 1$), its T_C is between 580 °C (pure magnetite) and -150 °C (pure ulvospinel); and in the case of titanohaematite, its T_N is between 675 (pure haematite) and -218 °C (pure ilmenite) [4]. As the temperature of the kiln decreases, more magnetic domains change into a ferromagnetic state; and when they cool below their T_C or T_N, instead of remaining disordered, they preferentially orient themselves with the direction and sense of the surrounding magnetic field that is the EMF at that precise time and place.

1.2. Earth's magnetic field (EMF)

Earth has its own magnetic field generated inside [3]. EMF is created by convection currents of molten iron and nickel, that make up the outer core of the Earth, due to the temperature difference between the upper part of the inner core (6000 °C) and the lower part of the mantle (3500 °C) [3]. These convection currents have a certain symmetry and are mainly described by a dipole field with its axis almost aligned with the geographical north-south axis (Fig. 1).

The EMF lines follow a toroidal geometry and are usually represented as a vectorial field. The description of the magnetic field in each geographical region is usually given by the inclination, declination and intensity of the magnetic vector, defined as a consequence of vectorial field of EMF. The inclination (Inc) is the angle between the vector and the horizontal or surface plane. The declination (Dec) is the angle between the horizontal projection of the vector and the geographic north, and takes positive values to the East [3]. EMF intensity (Int) is the magnitude or modulus of the EMF at each geographic coordinate. The intensity is higher near the poles, since there is more field lines density;

and lower near the equator, since the field lines density is lower (Fig. 1) [3]. Therefore, the magnetic field is different in each geographical position (Fig. 1) following a geometry relatively similar to a toroidal dipole, centred but inclined at a certain angle relative to the Earth's rotation axis (the dipole field corresponds to 90 % of the EMF).

The position of the magnetic north and south poles changes over time and hardly ever coincides exactly with the geographical north and south poles, although they move in their vicinity. The magnetic poles show two main types of movements: secular variation and geomagnetic reversals. Secular variation is the movement of the magnetic poles around the geographic poles. This variation is produced by changes in the core convection currents. Secular variation is a phenomenon that occurs constantly, although its speed is very slow on a human scale (≈ 17 km/ year) [7]. This variation is mainly produced by the non-dipole field contribution, generated by some changes in the core convection currents, distorting the almost toroidal dipole geometry. Geomagnetic reversals consist of transitions between "normal polarity" (magnetic south pole next to geographic north pole) and "reverse polarity" (magnetic north pole next to geographic north pole). Geomagnetic reversals are produced by a change in the direction of rotation of the outer core convection currents. Geomagnetic reversals are phenomena that occur less frequently than secular variation and have a highly variable period that ranges between several hundreds of thousands of years and several hundreds of millions of years [8]. That is why they are generally used in geology to identify long geological periods, while secular variations are useful in shorter periods of time [8].

The study of the EMF evolution throughout history is called paleomagnetism. This has been possible thanks to the monitoring of the different geological strata, where the different geomagnetic reversals and their chronology have been attested. These geomagnetic reversals have been especially important in the study of plate tectonics [9]. However, it has not only been studied for time periods on a geological scale. The monitoring of the secular variation has allowed to reconstruct the evolution of the EMF during the last millennia [10]. This has been possible thanks to the in-depth study of the direction in many samples of known chronology. Thanks to this reconstruction, the declination, inclination and intensity of the EMF can be estimated at any geographical point and for any chronology within the last three millennia [11]. In this way, for example, it is possible to date archaeological samples subjected to heating, as their TRM preserved the direction of the magnetic field on the date of the last heating [11]. Therefore,

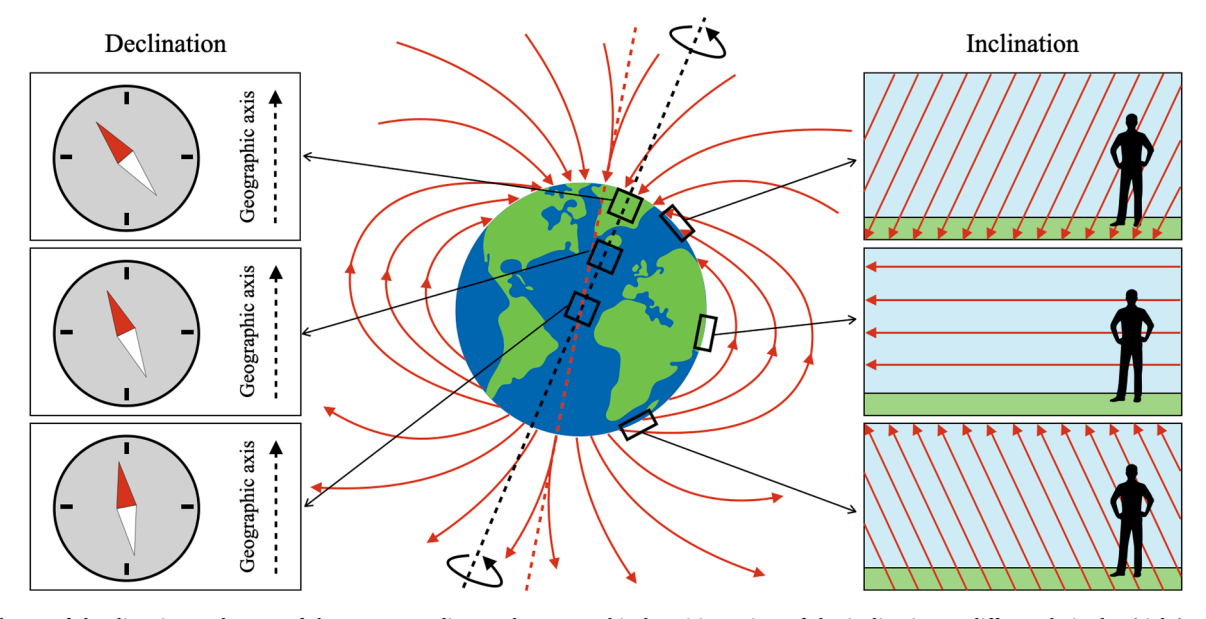


Fig. 1. Scheme of the direction and sense of the EMF according to the geographical position. View of the inclination at different latitudes (right). View of the magnetic declination at different latitudes (left). The dashed black line represents the Earth's axis of rotation and the dashed red line the EMF axis.

it is required that the sample has not been moved or displaced since then and to know the orientation (inclination and declination) and intensity of its remaining magnetism. This technique is called archaeomagnetic dating [12–14]. The three-dimensional vector that describes the direction of the remanent magnetism of archaeological samples (that take into account inclination and declination) is known as Characteristic Remanent Magnetization (ChRM).

In recent years, thanks to the numerous records of paleomagnetic data from samples of known chronology, it has been possible to reconstruct the EMF along history in great detail allowing the development of accurate and precise regional secular variation curves [11]. The archaeomagnetic dating process uses these secular variation curves once they are established. In them, values of the declination, inclination, and sometimes intensity, values of a sample with unknown chronology, are extrapolated. From these extrapolation actions a probability function is obtained, and with it, the dating and its uncertainty are calculated.

Our hypothesis starts from this point, but proposes to invert the archaeomagnetic dating process. The objective is to predict the original position of any object from its chronology and characteristic remanent magnetism (ChRM). While archaeomagnetic dating using magnetic direction requires samples obtained *in situ* (without displacement after heating), its reverse application would apply to samples that have not been found *in situ*, and therefore their original position is unknown. This application could be interesting in different cases, such as the reconstruction of burned structures, like fireplaces, kilns, furnaces, burnt floors, potteries, bricks or tiles. One example of this application has been discussed in this article. Specifically, the orientation of the tiles in the pavements of Tiebas Castle during the fire happening in 1378.

1.3. Architecture of Tiebas Castle: layout of the building and pavements

The Tiebas Castle was built between 1254 and 1266 by Teobaldo II of Navarra, V Count of Champagne as one of its palaces in the old Kingdom of Navarra (Spain). Tiebas Castle was a rectangular building measuring 49×27 m, with two floors, ground (0) and first (1), and divided into three blocks: south wing (SW), a porticoed patio (PP) and north wing (NW) (Fig. 2a and 2b). The ground floor was used for public functions (reception hall, archive, armoury...), while the first floor was used as the private quarters of the kings [15].

In the north wing and porticoed patio, the first floor was supported by a wooden framework. In the south wing, a massive stone vault of the ground floor served as the floor for the first. The only pavements that have been preserved are those of the ground floor of the north wing (tile pavement) and the patio (stone slabs pavement). The flooring on all the first floor and on the ground floor of the south wing have not been preserved.

The pavement on the ground floor of the north wing was found *in situ* between 2006 and 2009 [16]. However, the preserved part of the flooring was 24.2 % of the hall's surface. Based on the preserved part, it can be deduced that the pavement was structured in at least two main types of tile grids: one aligned orthogonally with the walls of the hall (which was called ORTH) (Fig. 2c) and another oblique at 45° (which will be called OBL) (Fig. 2c). These two types of grids have also been observed in other pavements in France made by these same craftsmen [17]: Reims, Soissons, Hautvillers, Saint-Imoges and Orbais-l'Abbaye.

Four different areas were distinguished on the pavement on the ground floor of the north wing (Fig. 2c): one large oblique (OBLa), one large orthogonal (ORTHa), one little oblique (OBLb) and one little orthogonal (ORTHb). Both, ORTHa and OBLa grids featured sets of 16

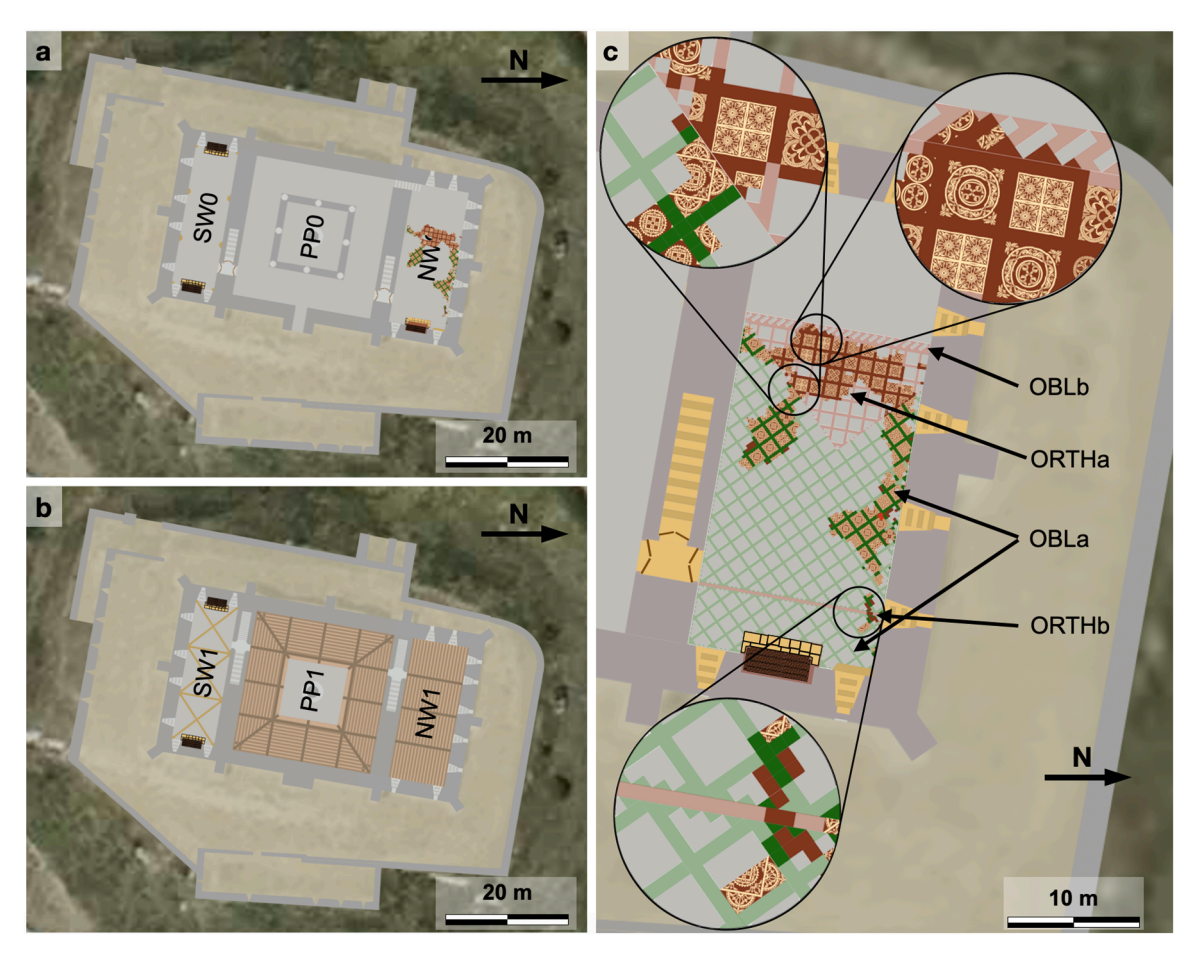


Fig. 2. General schematic zenithal view of the ground floor (a), first floor (b) and detail of the paving of the north wing (c).

dichromatic (4 \times 4) tiles separated by a single row of monochromatic tiles. The OBLb grid, located at the west end of the pavement, differs from the other two in that the dichromatic tiles are arranged in lines of three dichromatic tiles separated by monochromatic tiles. In the eastern part of the pavement there is a single line of dichromatic tiles arranged orthogonally and aligned to the walls (ORTHb).

The tiles had different sizes, composition or decoration depending on the grid (Table 1). ORTHa and OBLb grids were made up of 13.7×13.7 cm tiles, 2.5 cm thick, with a red paste and a light honey glaze. Motifs 1a, 1b, 2a, 3a, 4a, 4b, 5a, 5b, 6a, 7a, 7b, 8 and 12, were only settled in ORTHa and OBLb grids (Table 1). On the other hand, OBLa and ORTHb grids were made up by 14.6×14.6 cm, 2.2 cm thick and with two different compositions. Dichromatic tiles had red paste and a light honey glaze, and the monochromatic tiles had a yellowish paste and the glaze was greenish or yellowish. Motifs 9a, 10a, 10b, and 11 were found in OBLa and ORTHb grids.

In Fig. 2c, the grids found in situ virtually extended to complete the entire surface of the hall. In this way, the exact number of tiles that each of the grids could be estimated (Table 1). Considering these values (Table 1), it was observed that tiles with dimensions $14.6 \times 14.6 \times 2.2$ cm constituted the majority in this pavement, compared to those with dimensions $13.7 \times 13.7 \times 2.5$ cm. If the missing tiles are calculated according to the total area of the four grids: 85 % of missing dichromatic tiles would have dimensions of $14.6 \times 14.6 \times 2.2$ cm, while 15 % of the tiles would have dimensions of $13.7 \times 13.7 \times 2.5$ cm. However, these proportions did not coincide with the frequencies found in the tiles that have appeared in secondary position (not found in situ in a pavement): of the 505 dichromatic tiles found, only 7 % had dimensions of $14.6 \times 14.6 \times 2.2$ cm, while 91 % had dimensions $13.7 \times 13.7 \times 2.5$ cm (Table A1, Supplementary Material). This frequency was repeated in all the areas around the castle that have been intervened (Table A1, Supplementary Material). The two most plausible explanations are that the floor was not as expected (Fig. 2c) or that some other hall had a tile pavement in which $13.7 \times 13.7 \times 2.5$ cm tiles were the majority.

In addition to the 17 decorative motifs found *in situ* in these four grids, another 16 decorative motifs have not been found *in situ* (1c, 1d, 2b, 3b, 6b, 7c, 7d, 9b, 13, 14, 15, 16a, 16b, 17, 18 and 19) so it is unknown if they come from this pavement or another in other halls of the castle. The dimensions (size and thickness) allowed to hypothesise about its belonging to one or another grid (Table A1, Supplementary Material), as all the tiles from one grid must have the same size to fit.

1.4. The fire of August 1378

In August 1378 the castle was set on fire by the troops of the Castilian army [15]. The wooden structure of the roof of the entire building collapsed, setting fire to the wooden framework of the first floor (patio and north wing), which in turn collapsed on the ground floor. The only hall that was not affected by the fire was the ground floor of the south wing as it was vaulted. During the fire, both the walls and floors of the Castle were heated at high temperatures. Proof of it is the reddening of

Table 1
Summary of the characteristics of each grid of the pavement of NW0 hall. Abbreviations: PresM preserved monochromatic tiles; PresD–dichromatic tiles; ExpeM–estimate monochromatic tiles; ExpeD–estimated dichromatic tiles.

Grid	PresM	PresD	ExpeM	ExpeD	Size (cm)	Motifs
OBLa	316	566	1917	2979	14.6×14.6×2.2	9a 10a 10b 11
ORTHa	273	436	550	868	13.7×13.7×2.5	1a 1b 2a 3a 4a 4b 5a 5b 6a 7a 7b 8 12
OBLb ORTHb	14 0	5 3	227 0	65 60	$13.7 \times 13.7 \times 2.5$ $14.6 \times 14.6 \times 2.2$	3a 4a 4b 10a 10b

the sandstone ashlars on all the walls except on the ground floor of the south wing (Fig. 3). It is expected that this heating was high enough for the magnetic minerals that made up the pavement tiles could be partially or completely demagnetized and after cooling down they would have acquired the direction of the local magnetic field.

In this way, the tiles could have presented three types of demagnetization profiles:

- 1. A single component related to the original kiln firing in 1254–1266 (when the castle was built), in those not heated by the fire of 1378.
- 2. A single component in those the temperature of the fire (1378) was enough to completely demagnetize the magnetic phases from the kiln firing (1254–1266), replacing the original one.
- 3. Two components in those the demagnetization of the initial component was partial. In those cases, the primary component would be related to kiln firing above 900 °C [18], with an unknown orientation; while the secondary component would be related to the fire when they were in a horizontal orientation on the pavement.

Only those tiles with two components of magnetization have been used for the reverse archaeomagnetic dating method described in this paper.

For the reverse application of archaeomagnetic dating, the regional EMFs of Tiebas Castle (latitude $(\phi)=42.697^\circ$, longitude $(\lambda)=-1.638^\circ)$ has been considered. The Spanish secular variation curve defined in Madrid predicts $Dec=5.0^\circ\pm1.3^\circ$ and $Inc=45.2^\circ\pm1.1^\circ$ at this place in 1378 [19]. The corresponding values at Tiebas Castle obtained by the conversion through the Virtual Geomagnetic Pole (VGP) are $Dec=5.7^\circ\pm1.4^\circ$ and $Inc=48.2^\circ\pm1.0^\circ$ [20]. This direction is expected in tiles that cooled in situ during the 1378 event and were preserved in this position since.

The hypothesis that was considered is that there could have been other tiled pavements in other halls of the castle (Fig. 2). Listed below are the possibilities and the magnetic profile they could retain:

- A possible pavement in the ground floor of the south wing (SW0), under the stone vault, would not have been heated so they would only contain the primary component.
- A possible pavement on the first floor, on the wooden framework (NW1/PP1), would have a secondary component with a random direction, since the cooling down would have occurred after the collapse of the framework, when the tiles would have fallen and were scattered.
- The paving tiles on the ground floor of the north wing (NW0) and a
 possible pavement on the vault of the south wing (SW1) would have
 a secondary component with a direction compatible with a horizontal orientation. This orientation could be aligned orthogonally or
 oblique at 45° with respect to the walls.

The opposite hypothesis that was considered is that only the pavement of the ground floor of the north wing existed. So all tiles should have a secondary component. Furthermore, this secondary component should have an inclination and declination compatible with the local EMF and oriented like the four types of grids described above.

Therefore, the objective of this work was: - To reconstruct the possible tile pavements of the Tiebas Castle. - To determine the hall in which they were located and their orientation. - To determine the maximum temperature that each tile reached during the fire of 1378.

2. Materials and methods

2.1. Materials

The analysed samples were selected trying to cover the motifs already found *in situ* and those that were found in secondary positions (not *in situ*) (Table 2). In this study, 29 fragments of tiles were analysed:

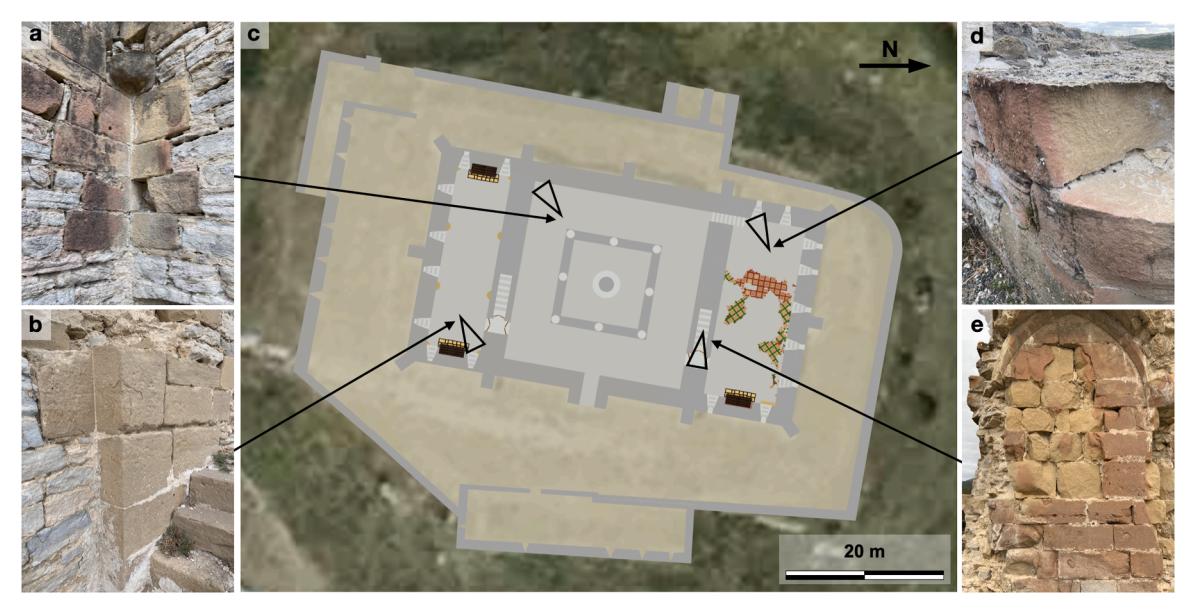


Fig. 3. Reddening of the surface of some sandstone ashlars affected by the 1378 fire (a, d, e) and its distribution in the building (c). The ashlars on the ground floor of the south wing are the exception (b), since the vault protected them from the fire.

Table 2
Description of tile samples studied, the analytical techniques applied on each one and the number of analyzed specimens per sample. Abbreviations: D-dichromatic tile; M-monochromatic tile; Dec.-Decoration; HSC-hermitage of Santa Catalina; UC-underground cellar; IW-internal wall; CF-crop field; NW-pav-northern hall pavement; ORTHa-orthogonal grid a; OBLa-oblique grid a; XRD-X-Ray Diffraction; XRF-X-Ray Fluorescence; Col.-Colorimetry; unk-unknown; IRM-TH-IRM Thermal demagnetization; TH-Thermal demagnetization.

Code	Size	Type	Dec.	Site	Grid	XRD	XRF	Col.	IRM-TH	TH
M11	14.6×14.6×2.2	D	10b	HSC	?	-	-	-	-	3
M12	$14.6 \times 14.6 \times 2.2$	D	10b	HSC	?	1	1	3	1	2
M15	$13.7 \times 13.7 \times 2.5$	D	15	HSC	?	1	1	3	1	2
M16	$13.7 \times 13.7 \times 2.5$	D	15	HSC	?	1	1	3	1	2
M23	$13.7 \times 13.7 \times 2.5$	D	4a	UC	?	-	-	-	-	3
M32	?	D	6b	HSC	?	1	1	3	1	2
M33	$14.6 \times 14.6 \times 2.2$	D	11	HSC	?	-	-	-	-	3
M1-13	$13.7 \times 13.7 \times 2.5$	D	unk	IW	?	-	-	-	-	3
M1-21	$13.7 \times 13.7 \times 2.5$	D	14	IW	?	-	-	-	-	3
M1-22	$13.7 \times 13.7 \times 2.5$	D	2	IW	?	-	-	-	-	3
M1-24	$13.7 \times 13.7 \times 2.5$	D	13	IW	?	-	-	-	-	3
M2-01	$13.7 \times 13.7 \times 2.5$	D	1a	CF	?	-	-	-	-	3
M2-02	$14.6 \times 14.6 \times 2.2$	D	9a	CF	?	-	-	-	-	3
M2-03	$14.6 \times 14.6 \times 2.2$	D	11	CF	?	1	1	3	1	2
M2-04	$13.7 \times 13.7 \times 2.5$	D	5b	CF	?	-	-	-	-	3
M2-05	$13.7 \times 13.7 \times 2.5$	D	8	CF	?	-	-	-	-	3
M2-06	$13.7 \times 13.7 \times 2.5$	D	3b	CF	?	1	1	3	1	2
M2-07	$13.7 \times 13.7 \times 2.5$	D	2	CF	?	-	-	-	-	3
M2-08	$13.7 \times 13.7 \times 2.5$	D	14	CF	?	-	-	-	-	3
M2-09	$13.7 \times 13.7 \times 2.5$	D	18	CF	?	-	-	-	-	3
M2-10	$13.7 \times 13.7 \times 2.5$	D	18	CF	?	-	-	-	-	3
M2-11	$13.7 \times 13.7 \times 2.5$	D	13	CF	?	-	-	-	-	2
M2-12	$13.7 \times 13.7 \times 2.5$	D	13	CF	?	-	-	-	-	3
P01-13	$13.7 \times 13.7 \times 2.5$	D	12	NW-pav	ORTHa	-	-	-	-	3
P01-17	$13.7 \times 13.7 \times 2.5$	D	12	NW-pav	ORTHa	-	-	-	-	3
P30-21	$13.7 \times 13.7 \times 2.5$	D	7b	NW-pav	ORTHa	-	-	-	-	3
P61-08	$14.6 \times 14.6 \times 2.2$	D	9a	NW-pav	OBLa	-	-	-	-	3
P61-10	$14.6 \times 14.6 \times 2.2$	M	m	NW-pav	OBLa	-	-	-	-	3
P73-13	$14.6 \times 14.6 \times 2.2$	D	11	NW-pav	OBLa	-	-	-	-	3

6 of those fragments were found *in situ* in the pavement of the ground floor of the north hall and the rest (23) in secondary positions: 6 in the hermitage of Santa Catalina (HSC), 1 in the underground cellar (UC); 4 around the internal wall (IW) and 11 in the crop fields around the castle (CF) (Fig. A1, Table 2 and Table A1, Supplementary Material). As mentioned above, the tiles at Tiebas Castle were classified according to their size and decoration. The size of these tile fragments in secondary position were $13.7 \times 13.7 \times 2.5 \, \mathrm{cm}$ in 17 samples and $14.6 \times 14.6 \times 2.2 \, \mathrm{cm}$ in 5 samples (Table 2). In them, the decorative

motifs were: 1a, 2, 4a, 5b, 8, 9a, 10b, 11, 3b, 6b, 8, 13, 14, 15, 18 (Table 2, Fig. 4).

2.2. Methods

This archaeometric study was carried out in two phases, the identification of the magnetic minerals present in the pastes and the directional study of the TRM (number of TRM components and determination of their inclination and declination values). For the identification of the

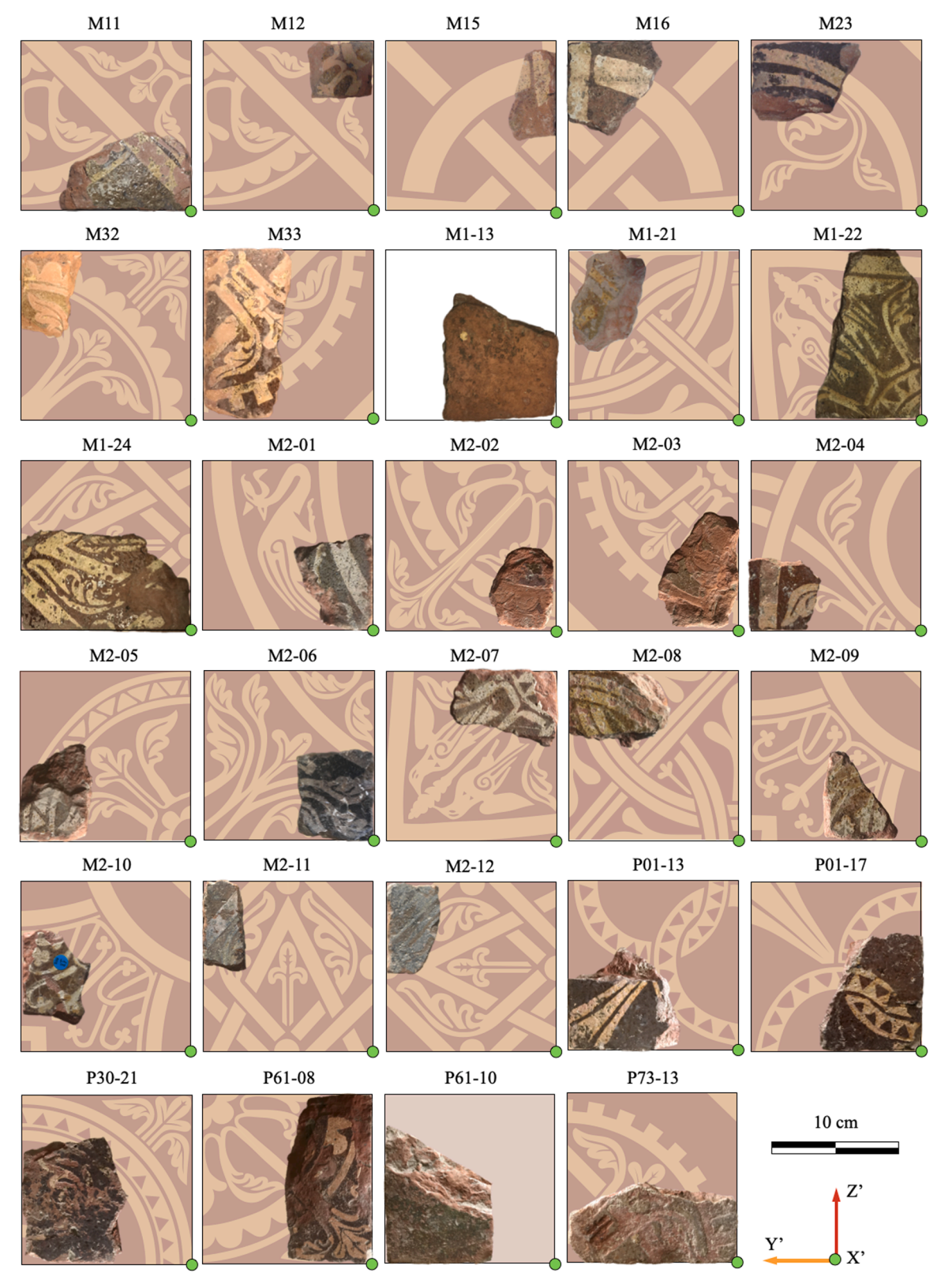


Fig. 4. Analysed tile fragments of carreaux de pavement from Tiebas Castle.

mineral phases, the samples were analysed by X-Ray Diffraction, X-Ray Fluorescence, colorimetry and Thermal Demagnetization on samples with three orthogonal IRMs acquired.

The mineral composition of some samples (Table 2) was determined by X-Ray Diffraction (XRD), with a Bruker D8 Advance diffractometer

with Cu K α radiation and an LYNXEYE XE-T detector. The experimental conditions for XRD experiments were: 2θ range from 5° to 70° , 2 s per step, and step size of 0.02° . The elemental composition of the polished surface of some samples (Table 2) has been analysed by X-Ray Fluorescence (XRF), using a Bruker S2 Puma instrument with a silver anode,

through a 4 μ m polypropylene filter and under a helium atmosphere. The measurement conditions were triplicate scans at 20 kV, 40 kV, 50 kV, 50 s per scan and a detector resolution of 10.8 eV (at 20 kV). The quantification was done with *Spectra Results Manager* software. Colorimetric analysis was performed with a CM-2300d Konica Minolta portable colorimeter with a xenon lamp (D65). For all the experiments, the CieL*a*b* colour parameters were measured in triplicate. The magnetic minerals of these fragments (Table 2) was also studied using Thermal Demagnetization of three orthogonal IRM acquired in 1.5 T, 0.4 T and 0.2 T fields [21]. For the TH Demagnetization the following temperatures were used: 75, 100, 125, 150, 200, 250, 300, 350, 400, 450, 500, 550, 600, 680 °C.

For the estimation of the TRM directions each sample was referenced with respect to its sides, taking two consecutive sides as the Y' and Z' axes (Fig. 4). The X' axis was defined as the ascending vector perpendicular to the decorated plane of the tile (Fig. 4). From each sample, between 2 and 3 cubes of around 1 cm³ were cut orthogonally to the defined axes. The samples were demagnetized by heating/cooling cycles in a magnetic shielding tube furnace heating between 100 and 600 °C with 25 °C step and the remanent magnetization after each step were measured using a JR-6 Spinner Magnetometer. The results were analysed using PaleoMac 6.5 software [22]. The results were represented using Zijderveld diagrams and the number of components and their demagnetization temperature ranges were identified [23]. Declination and inclination, and $\alpha 95$ (95 % dispersion angle of the Fisherian distribution) of the components of each sample were obtained by using Principal Component Analysis [24]. As the samples were not found and referenced with respect to their original position, but rather were referenced with respect to their sides, declination and inclination values must be considered relative.

Sometimes the TRM direction can be biased by anisotropy effects because the magnetic grains are preferentially oriented in some preferential direction or plane. This greater anisotropy is common, for example, when the material has been formed by sedimentation or if the material has suffered some type of mechanical compression in some direction. In the case of mould-stamped tiles such as *carreaux de pavement*, it can be significant in the flattening plan of the tile, resulting in a weaker acquisition along the thickness i.e. z'-axis [25,26]. This anisotropy would above all modify the relative inclination of the TRM, so it must be taken into account.

To evaluate the TRM anisotropy effect, the TRM anisotropy tensor was determined for each sample. This TRM tensor was obtained from the acquisition of six TRM by applying a field of 50 mT, at 500 °C successively in six different directions relative to the samples (X', -X', Y', -Y', Z', -Z'), generally when $\sim\!60-\!90$ % of Natural Remanent Magnetization (NRM) were demagnetized [27]. The correction factor f was calculated from the TRM anisotropy tensor as defined by Veitch et al., 1984 [28]. The effect of TRM anisotropy was corrected for all relative inclinations by the following equation [29], were I_0 was the original relative inclination, I_F was the experimentally obtained relative inclination and f was the flattening factor (defined as the ratio between the K_{min} (K_{XX}) and the K_{max} (K_{YY} or K_{ZZ}), where K_{XX} , K_{YY} and K_{ZZ} are the three axis of the TRM anisotropy tensor.

$$tan I_0 = f tan I_F (1)$$

The effect of TRM anisotropy was also corrected for all relative declinations by the following equation, were D_0 was the original relative declination, D_F was the experimentally obtained relative declination and L was the lineation factor (defined as the ratio between the K_{int} (K_{YY} or K_{ZZ}) and the K_{max} (K_{YY} or K_{ZZ}).

$$tan D_0 = L tan D_F (2)$$

3. Results and discussion

3.1. Identification of magnetic minerals

The samples for characterization were selected according to the criterion of covering the entire range of NRM intensities (Table 3): from 0.3 A/m to 31 A/m. The objective was to determine which minerals were responsible for a greater or lesser remaining intensity, as well as to know the origin that causes it.

As a first step to determine the magnetic properties of the Tiebas *pavement carreaux*, the presence of magnetic minerals was studied. Samples of tile fragments M12, M15, M16, M32, M2–03 and M2–06 were analysed by XRF and XRD. XRF analysis showed iron-based compounds, expressed as Fe_2O_3 , ranging from 3.4 % to 4.4 % (Table 3). In previous publications, some magnetic minerals were identified in these same *pavement carreaux* [18,30]. These iron oxides were in the form of haematite, mostly (Fig. 5). Haematite (H) was identified due to the presence of the following XRD reflections (PDF 33–0664): $2\theta = 24.1^{\circ}$ (012), 33.2° (104), 35.6° (110), 40.9° (024), 49.6° (024), 54.3° (116), 57.2° (018) and 62.6° (214) (Fig. 5).

Other iron-containing minerals were identified, such as spinel (S) or dehydroxylated muscovite KAl₃Si₃O₁₀ (DM) (Fig. 5). Both may contain some amount of iron oxides as impurities. The presence of dehydroxylated muscovite (PDF 46-0741) was detected in M12, M32 and M2-03 samples through the $2\theta = 19.7^{\circ}$ (110), 22.7° (-113), 34.6° (131) and 61.3° (315) reflections (Fig. 5). M12, M15, M16 and M2-06 had spinel (PDF 05–0672) content due to the $2\theta = 31.3^{\circ}$ (220), 37.0° (311) 45.0° (400), 59.3° (511) and 65.6° (440) reflections (Fig. 5). Samples that contain high amounts of dehydroxylated muscovite didn't have spinel and vice versa (Fig. 5). This could be due to the temperature that reached each sample during kiln firing. The tiles fired at lower temperature (850-900 °C) contained dehydroxylated muscovite and the tiles fired at higher temperature (950-1000 °C) contained spinel. Dehydroxylated muscovite could contain Fe²⁺ ions and has no magnetic properties. Magnesium spinels could contain Fe³⁺ ions, such as $(Mg_{1.7}Fe_{0.23})Al_{1.97}O_4$, with magnetic properties [31]. M12, M15, M16, M2-03 and M2-06 showed reflections that could be compatible with magnetite $Fe_2^{2+}Fe_2^{3+}O_4$ (Mn) (PDF 19-0629) and maghemite $Fe_2^{3+}O_3$ (Mh) (PDF 39-1346), although this could not be confirmed in all of them as they coincide with some of the reflections of haematite ($2\theta = 35.6^{\circ}$, 54.3°, 57.2° and 62.6°) (Fig. 5). Sample M2–06 was the only one in which some haematite reflections ($2\theta = 24.1^{\circ}$, 33.2° , 40.9° and 49.6°) were not detected. On the contrary, common reflections ($2\theta = 31.1^{\circ}$ (220), 35.6° (331), 37.1° (222), 43.2° (400), 54.5° (422), 57.2° (511) and 62.6° (400)) with magnetite and maghemite were detected, so it is confirmed that at least this sample contained some of the latter minerals.

Elemental analysis of XRF showed the presence of titanium (0.5-0.6%), which has only been detected in the form of rutile (non-magnetic) in XRD. Elemental analysis also showed the presence of Mg (1.0-1.5%). This magnesium could be found in some samples (M12, M32 and M2-03) in the form of dehydroxylated muscovite, and in others in the form of spinel (M15, M16 and M2-06).

The colour of the samples turned out to be related to the firing conditions (temperature and atmosphere) [18]. Sample M2–06 had a greyish colour with lower L*a*b* coordinates than the others (Table 3). Samples M12, M15 and M16 showed a reddish brown colour (Table 3). Sample M32 was lighter in colour and M2–03 is an intermediate point between the latter and the previous ones (Table 3).

The thermal demagnetization of the three-component IRM showed (Fig. 6) that most of the intensity corresponded to the x-axis (0.2 T), and lesser to the z-axis (1.5 T) and y-axis (0.4 T). The intensity relative to hematite should be found in the z-axis (1.5 T), since the remanent magnetization saturates between 1.5 and 5 T [21]. However magnetite would be producing the intensity of the x-axis (0.2 T) and y-axis (0.4 T), as the remanent magnetization of this ferromagnetic mineral

Table 3

Characterization of magnetic minerals: NRM intensity (A/m), relative abundance of dehydroxylated muscovite ($2\theta = 19.8^{\circ}$), haematite ($2\theta = 33.2^{\circ}$), spinel ($2\theta = 65.6^{\circ}$) and haematite or magnetite or magnetite or magnetite ($2\theta = 35.6^{\circ}$), HCS, abundance (% w/w) of Fe, Mg and Ti oxides and CIEL*a*b* coordinates. The relative abundance is expressed as the count intensity ratio of the maximum reflection of the mineral and the maximum reflection of quartz (PDF 33–1161, at $2\theta = 26.6^{\circ}$). Abbreviations: DM-dehydroxylated muscovite; H-haematite; S-spinel; and H-Mn-Mh-haematite or magnetite or magnetite, HMC-haematite crystal size.

ID	NRM Intensity (A/m)	XRD				XRF			Colour		
		DM	Н	S	H-Mn-Mh	% Fe ₂ O ₃	% MgO	% TiO ₂	L*	a*	b*
M2-06	31 ± 2	0.019	0.012	0.041	0.035	4.6	1.3	0.62	37	6	18
M16	7.0 ± 0.5	0.019	0.032	0.043	0.037	3.4	1.3	0.60 %	46	24	33
M15	6 ± 1	0.028	0.029	0.035	0.038	4.7	1.0	0.59	42	24	33
M12	6.3 ± 0.5	0.022	0.038	0.037	0.042	5.3	1.1	0.63	44	22	32
M2-03	3.9 ± 0.5	0.025	0.017	0.011	0.023	4.2	1.0	0.54	50	23	34
M32	0.3 ± 0.2	0.047	0.028	0.019	0.031	4.2	1.2	0.58	49	29	43

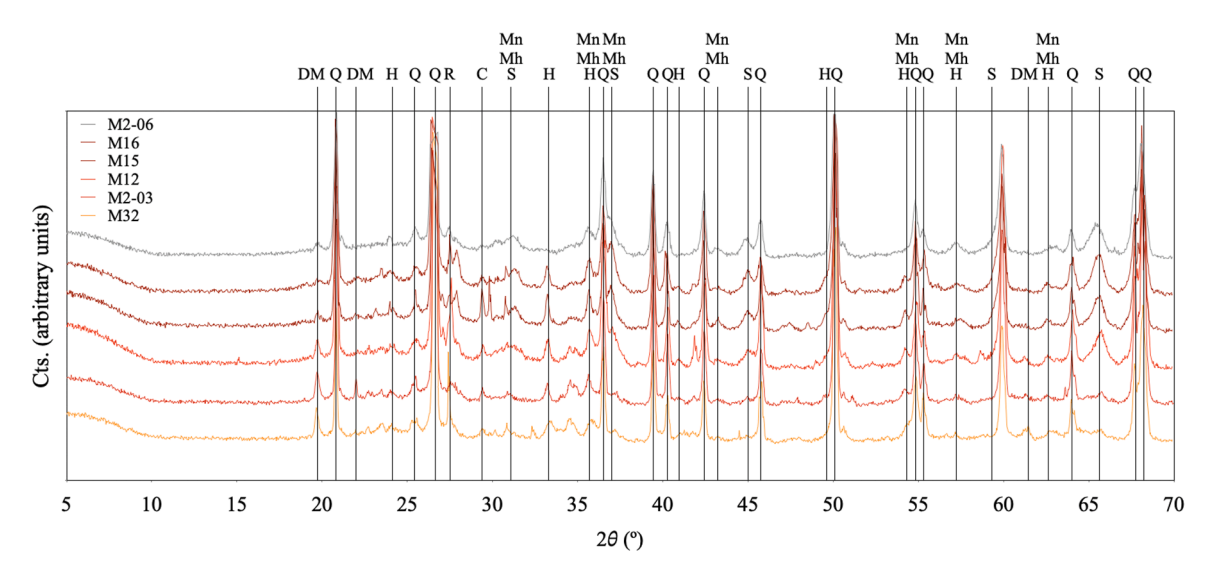


Fig. 5. X-ray diffraction patterns of the analysed samples. Abbreviations: Q-quartz (PDF 33–1161); R-rutile (PDF 21–1276); DM-dehydroxylated muscovite (PDF 46–0741); H-haematite (PDF 33–0664); C-calcite (PDF 05–0586); S-spinel (PDF 05–0672); Mn-magnetite (PDF 19–0629) and Mh-maghemite (PDF 39–1346).

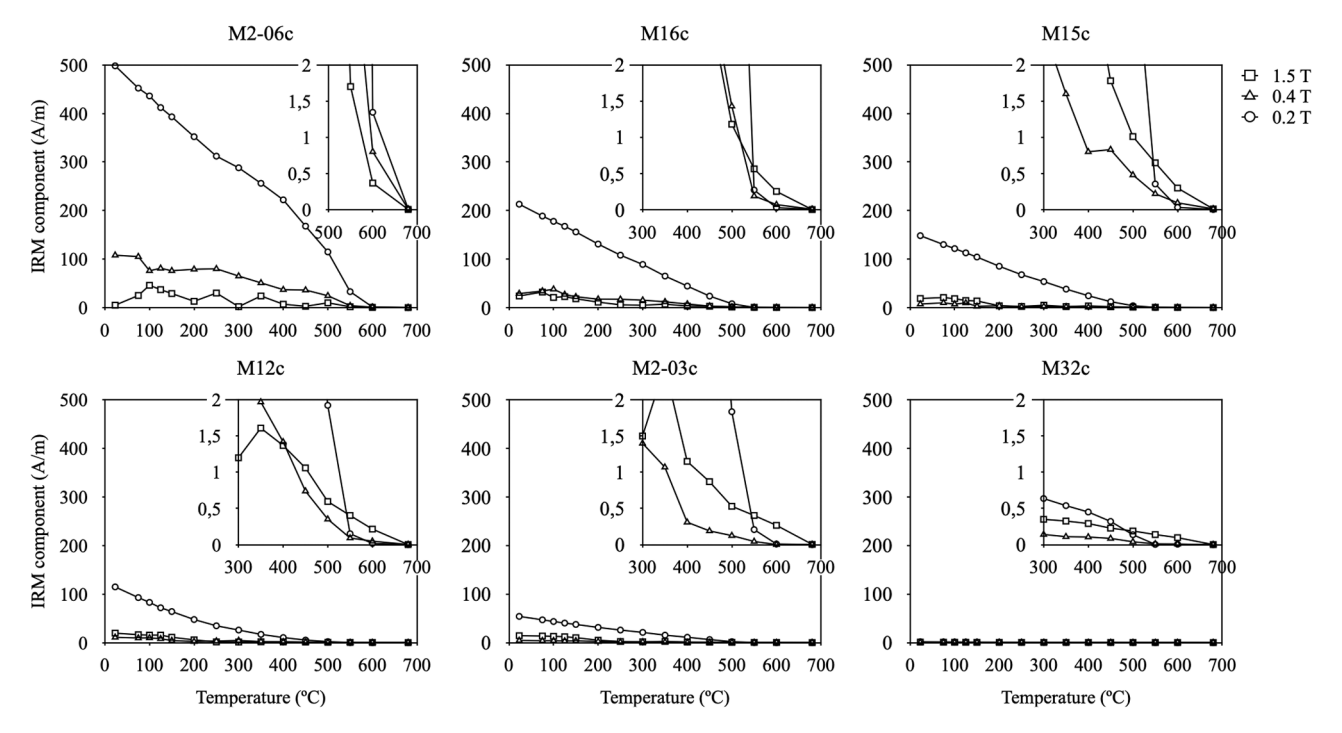


Fig. 6. Thermal demagnetization of a three-component IRM produced by magnetising the samples M2–06, M16, M15, M12, M2–03 and M32 in 1.5 T along its z'-axis, followed by 0.4 T, along the y'-axis, and finally 0.2 T along the x'-axis.

saturates around 0.3 T [21]. These results allowed to identify that between 95 % and 99 % of the remaining intensity was demagnetized before 600 °C, mostly in the direction of the x'-axis (0.2 T) and y'-axis (0.4 T). According to this result, most of the IRM is carried by magnetite, as its maximum unblocking temperature is 580 °C [21]. In all samples, except M2-06, the intensity of the z'-axis only exceeded that of the other two axes at 600 and 680 °C, when only haematite remained. Haematite has a maximum unblocking temperature of 675°C [21]. Sample M2-06 showed a significantly initial higher IRM intensity (509.6 A/m) (Fig. 6) 99.9% of it due to magnetite (intensity below 600 °C) and only 0.1 % due to haematite (intensity at 600 °C). In contrast, sample M32 showed a much lower initial intensity (1.9 A/m), 95 % of it due to magnetite (intensity below 600 °C) and up to 5 % of the intensity produced by haematite (intensity at 600 °C). All the samples had an intensity in the z'-axis at 600 °C of between 0.10 A/m and 0.37 A/m, so the amount of hematite would be much more homogeneous between samples than that of magnetite, which varied between 1.8 A/m and 509.2 A/m. A phase compatible with epsilon-iron oxide was also identified within the z'-axis (1.5 T) that completely disappeared at 250 °C. This phase with high coercivity (>0.4 T) and low unblocking temperature (around 200 °C) was identified in samples M16, M15, M12 and M2-03 [32], although its contribution to the IRM intensity was low (around 10 %). In sample M2-06 it was impossible to be identified due to interference in the y'-axis of the large amount of magnetite. In sample M32 epsilon-iron oxide was not detected.

The progression in the disappearance of dehydroxylated muscovite [21] and the formation of spinel, which were directly proportional to the NRM intensity, could indicate that it was proportional to the firing temperature [30]. Magnetite could be generated from the iron (Fe²⁺) present in muscovite. In the case of sample M2-06, the temperature was not a sufficient cause to reach such a NRM intensity, so it could be also due to a reducing atmosphere during firing. This reducing atmosphere would have reduced much of the haematite to magnetite. The colour of the samples turned out to be proportional to the amount of magnetite as the red colour darkened to grey. The colour was therefore also dependent on the firing conditions (temperature and atmosphere). It was also concluded that the remnant intensity was mainly due to the presence of magnetite in the samples, as shown from the three component IRM. Magnetite could have been in very low concentrations in relation to that of haematite, however, as the saturation magnetization of magnetite is around 200 times higher than that of hematite, its contribution to magnetization is major.

3.2. Study of the orientation of magnetic components

The Zijderveld diagram of Fig. 7 represents how the 3-axis projection of the magnetic intensity changes as the demagnetizing temperature was increased.

The study of the orientation of the magnetic components (Fig. 7) allowed to identify two magnetic components in 100 % of the samples found *in situ* (P01–13, P01–17, P30–21, P61–08, P61–10 and P73–13). In the samples not found *in situ*, 11 presented a single component, while 12 presented two components (Table 4). Once the number of components were identified, to obtain the direction of each of them, a Principal Component Analysis was carried out [24]. The direction of the TRM components was calculated as the mean of the 2–3 specimens of each sample. In the samples with two components, the temperature of junction between the two components was determined (Table 5).

The Relative Declination (RDec) and Relative Inclination (RInc) obtained from Characteristic Remanent Magnetization (ChRM) were adjusted to take into account the limitations of sampling orientation and also to correct the TRM anisotropy effect. While sampling those samples not found in situ, the choice of the reference axes was made arbitrarily, so in fact any of the four corners could have been the origin of the ordinate. That is why all RDec have been reduced to the first quadrant (0-90°): RDec' (Table 4). The RDec' value (Table 4) also included the correction of the TRM anisotropy effect in the relative declination. However, this correction was very small since there was almost any anisotropy between the Y' and Z' axes (tile horizontal plane). The inclination shallowing was also corrected in all the relative inclinations (RInc) by determining the anisotropy of the remanent magnetization. In this case, the effect of the anisotropy in the x' axis was significant, compared to the other two, so the correction of the RInc was between \pm 8°. The corrected relative inclination was expressed as RInc' (Table 4). From now on the Relative Declination and Relative Inclination values that were used were: RDec' and RInc'.

For the interpretation of the direction results, the samples found *in situ* on the NW0 hall were taken as reference (Fig. 8). The three samples belonging to the ORTHa grid (P01–13, P01–17 and P30–21) had an average relative declination (RDec') of 81.3°, or 351.3° if we take into account its original quadrant (+270°). On the other hand, those on the OBLa grid (P61–08, P61–10 and P73–13) had an average relative declination of 43.3° in the second component, or 358.3° if we consider its original quadrant (+270°) and oblique orientation (+45°). At this point it is important to take into account that the castle walls were not oriented exactly north so they have a turn towards the east of 11.5° (Fig. 2). So the real declination was 2.8° (351.3° + 11.5°), for ORTHa, and 9.8° (358.3° + 11.5°), for OBLa. As said before, the theoretical declination at the Castle place in 1378 was 5.7° \pm 1.4°, so both values were around the expected ones.

Regarding the relative inclination, it was assumed that the relative inclination was equivalent to the real inclination as they were placed horizontally in the pavement. The average inclination of the six samples was 49.8° in the second component, the theoretical one being 48.2° \pm 1.0°.

In those samples with a single component it should be checked

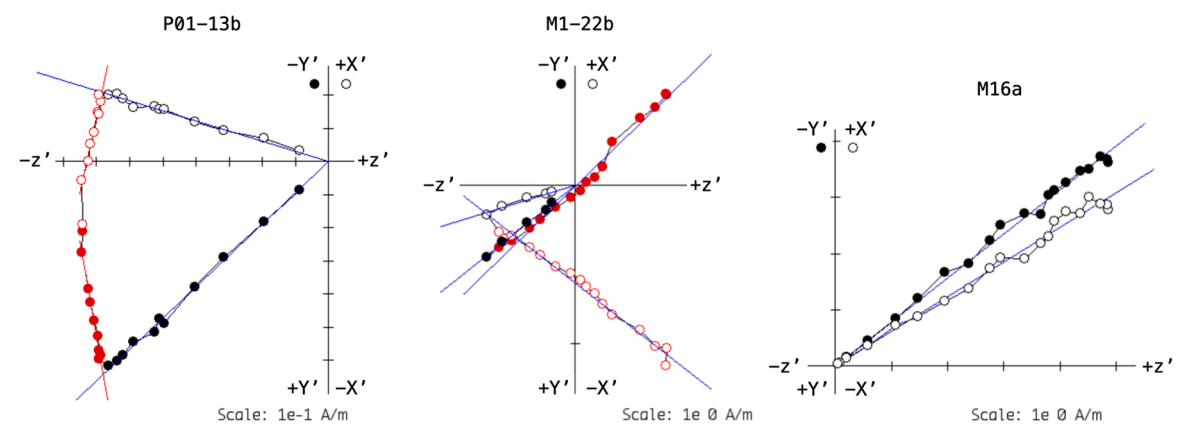


Fig. 7. Zijderveld diagram of samples with two components (P01-13b and M1-22b) and one single component (M16a).

Table 4
Directional parameters for the primary and secondary components of each sample. Abbreviations: n–number of specimens per sample; RDec–relative declination; RInc–relative inclination; α95–95 % dispersion angle of the Fisherian distribution; RDec'–corrected relative declination; RInc'–corrected relative inclination.

ID	n	Primary con	nponent		Secondary component						
		RDec (°)	RInc (°)	α95 (°)	RDec' (°)	RInc' (°)	RDec (°)	RInc (°)	α95 (°)	RDec' (°)	RInc' (°)
M11	3	108	-43	7	18	-49	-	-	-	-	-
M12	2	312	+10	4	42	+12	-	-	-	-	-
M15	2	236	-24	4	55	-29	-	-	-	-	-
M16	2	322	-26	1	51	-31	-	-	-	-	-
M23	3	45	-12	2	45	-14	177	+47	6	87	+52
M32	2	56	+34	10	55	+37	-	-	-	-	-
M33	3	2	-41	2	2	-46	-	-	-	-	-
M1-13	3	92	+36	2	2	+43	227	+35	23	46	+43
M1-21	3	255	+41	2	75	+49	49	+45	12	48	+54
M1-22	3	142	+13	2	53	+17	317	+29	5	49	+36
M1-24	3	278	-35	10	8	-43	278	-52	?	8	-60
M2-01	3	275	-31	13	5	-35	330	+35	4	62	+39
M2-02	3	148	-21	2	58	-23	-	-	-	-	-
M2-03	2	47	+21	6	49	+25	182	+33	9	2	+38
M2-04	3	253	+35	6	73	+35	225	+52	25	45	+53
M2-05	3	264	+37	2	84	+42	181	+5	19	1	+6
M2-06	2	307	0	1	37	0	-	-	-	-	-
M2-07	3	327	+23	3	57	+28	256	+32	2	76	+38
M2-08	3	290	-24	4	18	-27	-	_	-	-	_
M2-09	3	191	-39	3	12	-47	347	+64	1	76	+70
M2-10	3	92	-39	6	2	-45	177	-11	2	87	-14
M2-11	2	325	+16	12	52	+20	-	-	-	-	-
M2-12	3	218	+33	6	41	+36	-	-	-	-	-
P01-13	3	226	-13	2	45	-14	353	+41	3	83	+44
P01-17	3	107	-30	2	18	-37	350	+41	7	80	+49
P30-21	3	318	-11	3	47	-13	351	+42	8	81	+48
P61-08	3	321	+8	4	50	+10	307	+48	22	36	+54
P61-10	3	358	+35	7	88	+39	322	+43	26	51	+47
P73-13	3	327	-3	3	57	-3	311	+53	9	41	+57

Table 5
Directional parameters for the secondary component and Component Changing Demagnetization Temperature (CCDT) of each sample classified according to expected place and grid. Abbreviations: Dec.–Decoration.

ID	Dec.	Size	Place	Grid	RDec' (°)	RInc' (°)	Temp. (°C ± SD)
P01-13	12	13.7×13.7×2.5	NW0	ORTHa	83	+44	280 ± 30
P01-17	12	$13.7 \times 13.7 \times 2.5$	NW0	ORTHa	80	+49	300 ± 30
P30-21	7b	$13.7 \times 13.7 \times 2.5$	NW0	ORTHa	81	+48	310 ± 40
P61-08	9a	$14.6 \times 14.6 \times 2.2$	NW0	OBLa	36	+54	280 ± 30
P61-10	m	$14.6 \times 14.6 \times 2.2$	NW0	OBLa	51	+47	300 ± 30
P73-13	11	$14.6 \times 14.6 \times 2.2$	NW0	OBLa	41	+57	290 ± 10
M15	15	$13.7 \times 13.7 \times 2.5$	SW-0	?	-	-	-
M16	15	$13.7 \times 13.7 \times 2.5$	SW-0	?	-	-	-
M2-06	3b	$13.7 \times 13.7 \times 2.5$	SW-0	?	-	-	-
M2-08	14	$13.7 \times 13.7 \times 2.5$	SW-0	?	-	-	-
M2-11	13	$13.7 \times 13.7 \times 2.5$	SW-0	?	-	-	-
M2-12	13	$14.6 \times 14.6 \times 2.2$	SW-0	?	-	-	-
M11	10b	$14.6 \times 14.6 \times 2.2$	SW-0	?	-	-	-
M12	10b	$14.6 \times 14.6 \times 2.2$	SW-0	?	-	-	-
M33	11	$14.6 \times 14.6 \times 2.2$	SW-0	?	-	-	-
M2-02	9a	$14.6 \times 14.6 \times 2.2$	SW-0	?	-	-	-
M32	6b	?	SW-0	?	-	-	-
M2-03	11	$14.6 \times 14.6 \times 2.2$	NW0/SW-1	ORTH	49	+38	280 ± 20
M23	4a	$13.7 \times 13.7 \times 2.5$	NW0/SW-1	ORTH	2	+52	320 ± 20
M2-07	2	$13.7 \times 13.7 \times 2.5$	NW0/SW-1	ORTH	87	+38	450 ± 20
M1-13	?	$13.7 \times 13.7 \times 2.5$	NW0/SW-1	OBL	76	+43	250 ± 50
M1-21	14	$13.7 \times 13.7 \times 2.5$	NW0/SW-1	OBL	46	+54	290 ± 10
M2-04	5b	$13.7 \times 13.7 \times 2.5$	NW0/SW-1	OBL	48	+53	350 ± 40
M1-22	2	$13.7 \times 13.7 \times 2.5$	NW0/SW-1	OBL	45	+36	450 ± 20
M2-05	8	$13.7 \times 13.7 \times 2.5$	NW1/PP-1	?	1	+6	240 ± 10
M1-24	13	$13.7{\times}13.7{\times}2.5$	NW1/PP-1	?	8	-60	360 ± 60
M2-09	18	$13.7 \times 13.7 \times 2.5$	NW1/PP-1	?	76	+70	540 ± 10
M2-10	18	$13.7 \times 13.7 \times 2.5$	NW1/PP-1	?	87	-14	540 ± 10
M2-01	1a	$13.7{\times}13.7{\times}2.5$	NW1/PP-1	?	62	+39	550 ± 40

whether it corresponded to a primary or secondary component. In other words if it belongs to the heating during firing in the kiln or to the Castle fire in 1378. For this, the relative inclinations (RInc') were evaluated.

Only those with a positive sign and a value close to the calculated local EMF (Inclination $=48.2^{\rm o}\pm1.0^{\rm o})$ were considered as possible secondary components: M32, and M2–12. However, this possibility was ruled out

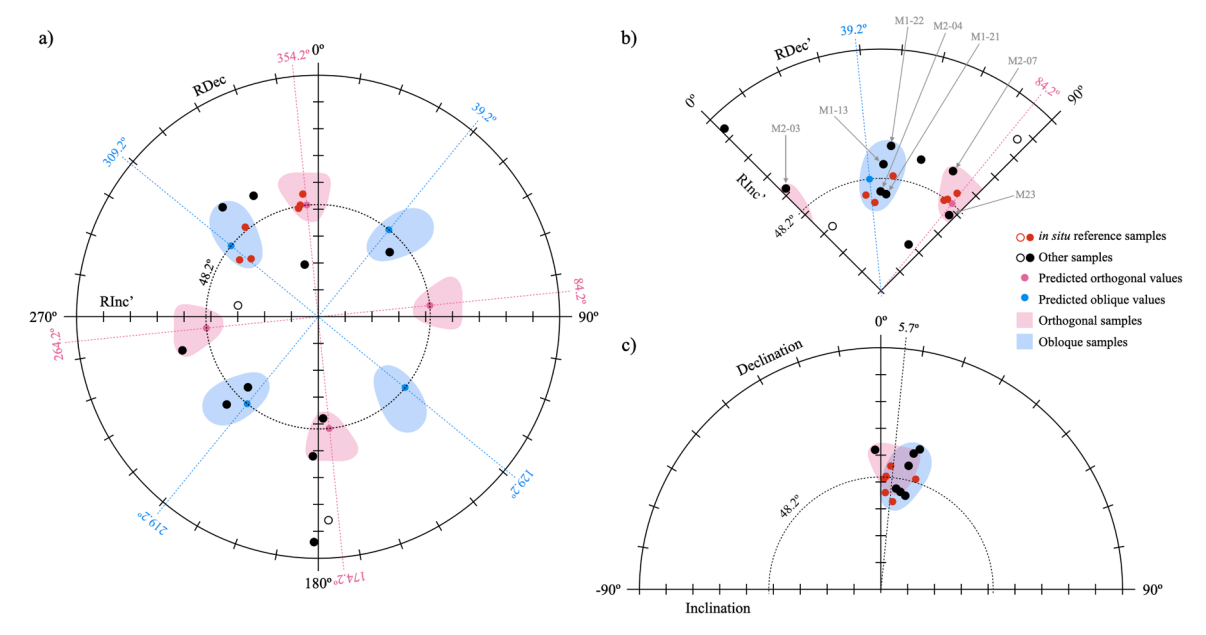


Fig. 8. Stereographic representation of the RDec and RInc' values, before reducing them between 0 and 90° (a). Stereographic representation of the RDec' and RInc' values (b). Stereographic representation of the Declination and Inclination with respect to the local EMF in 1378 (c). In light pink and light blue the areas of samples compatible with the hypothetical orthogonal (blue) and oblique (pink) values. In situ samples are displayed in red and others in black. Solid and open circles correspond to positive and negative inclinations, respectively.

in both cases since its relative inclinations (RInc') was below the expected value. Furthermore in both, relative declination and relative inclination, were compatible with a vertical position during stacking in the kiln. This question will be deeply discussed in another publication [33].

In those samples with two components, only the secondary component was considered. The samples were classified according to whether their direction was compatible with any of the NWO grids or not (ORTHa, ORTHb, OBLa and OBLb). For this, both the hypothetical direction of the EMF and the ChRM of the tiles found *in situ* were taken as a reference. In this way, samples M1–13, M1–21, M2–04 and M1–22 have a RInc' compatible with a horizontal position (RInc' between 36° and

54°) and a RDec' compatible with a placement on an OBL grid (RDec' between 45° and 49°) (Fig. 8). Samples M2–03, M23, and M2–07 have a RInc' compatible with a horizontal position (RInc' between 38° and 52°) and an RDec' compatible with placement on an ORTH grid (RDec' between 76° and 92°). On the contrary, samples M2–05, M1–24, M2–09, M2–10 and M23 have non-expected RDec' and RInc' values so they can not be associated with any horizontal position (Fig. 8). Therefore, neither with any grid of the NW0.

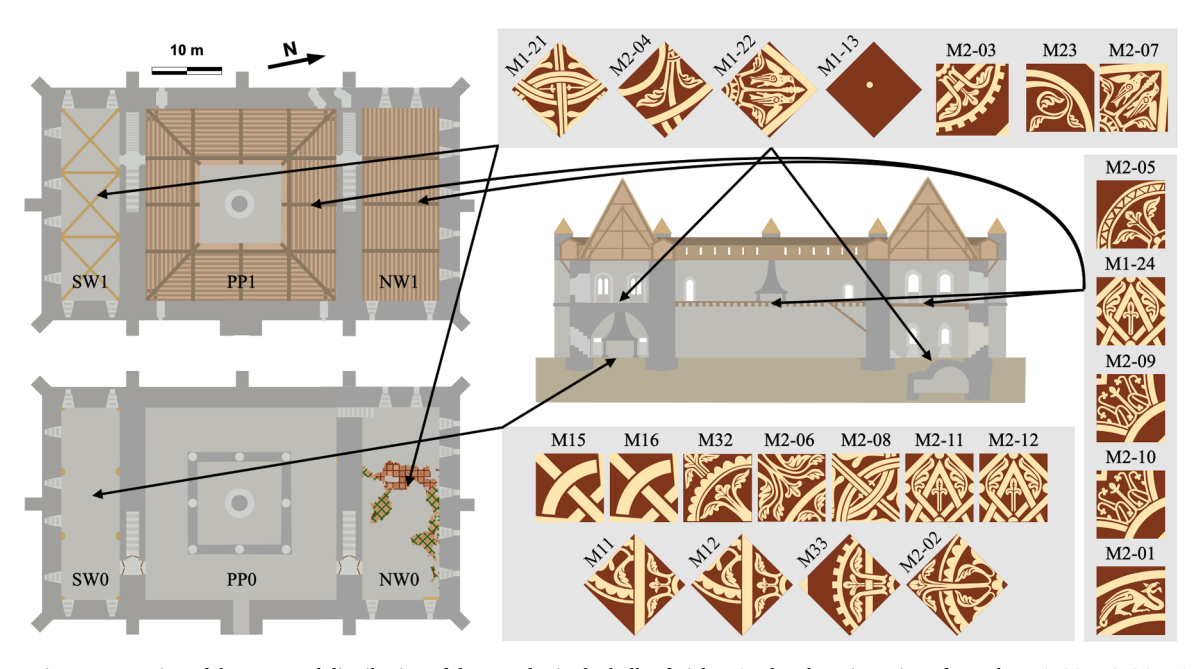


Fig. 9. Schematic representation of the proposed distribution of the samples in the halls of Tiebas Castle. The orientation of samples M1–21, M2–04, M1–22, M1–13, M2–03, M2–07 is according to the direction obtained. The rest of the samples have been oriented arbitrarily.

3.3. Tiebas Castle pavements

3.3.1. Pavement of the SWO hall

According to the previous results (Table 5), a total of 11 samples (M11, M12, M15, M16, M32, M2–02, M2–06, M2–08, M2–11 and M2–12) presented a single component and all of them were compatible with a primary component (kiln firing). As mentioned above, the only location of the castle in which the tiles did not suffer the effects of the fire is the ground floor of the south wing (SW0) (Fig. 9). No flooring has been preserved in this hall, so until now it was unknown how it was originally composed. The possibility that they were never installed in any pavement was ruled out since many of them retained remains of mortar at their base.

According to the sizes of these 11 samples (5 with $13.7 \times 13.7 \times 2.5$ cm size, 5 with $14.6 \times 14.6 \times 2.2$ cm size and 1 with unknown size), this pavement could have had two or more grids, similar to those found in the tile pavement of the ground floor of the north wing (NW0). However, the orientations of each one cannot be determined since their orientation was not recorded by the heat of the fire.

According to the decoration of the tiles from this group, all the motifs of size $13.7\times13.7\times2.5$ cm corresponded to those not found on the pavement of the NW0 hall. The decorations on the $14.6\times14.6\times2.2$ cm tiles matched the decorations on the pavement in the NW0 hall. Regarding the place where the samples were found, it should be noted that all the samples from the hermitage of Santa Catalina (HSC) would be associated with this pavement in hall SW0. The rest of the samples were found in the fields to the north and west of Castle hill.

3.3.2. Pavement of the NWO and SW1 halls

The seven samples (M1–13, M1–21, M1–22, M2–03, M2–04 and M2–07) compatible with a horizontal position (RInc' $\approx 48.2^{\circ} \pm 1.0^{\circ}$) could come from either NW0 or SW1 halls, or even from both (Fig. 9). Both halls were affected by the fire and its structure below did not collapse, remaining horizontal both during and after the fire. Their orientation allowed to distinguish at least three different grids: an OBL composed of $13.7 \times 13.7 \times 2.5$ cm tiles, another ORTH composed of $13.7 \times 13.7 \times 2.5$ cm tiles and another ORTH composed of $14.6 \times 14.6 \times 2.2$ cm tiles. The first of them (M1–13, M1–21, M2–04 and M1–22) would be compatible with the OBLb grid in hall NW0 (Fig. 2) or with another possible one in hall SW1. The second (M23 and

M2–07) would be compatible with the ORTHa grid in hall NW0 (Fig. 2 and Table 1) or, as well, with another analogous grid in hall SW1. The third, represented only by sample M2–03, would be compatible with the ORTHb grid in hall NW0 (Fig. 2) or with another analogous one in hall SW1. These tiles (M1–21, M2–04, M1–22, M23, M2–07 and M2–03) were the ones whose original orientation was determined (Fig. 9).

3.3.3. Pavement of the PP1 and NW1 halls

Samples M2–05, M1–24, M2–09, M2–10 and M2–01 are those with a direction not compatible with a horizontal position. These directions could be explained through the existence of a pavement on one of the wood frameworks on the first floor (Fig. 9). These could be located in the porticoed patio (PP1) or in the north wing (NW1). In all cases the size of the tiles is $13.7 \times 13.7 \times 2.5$ cm, so the existence of more than one grid cannot be confirmed.

3.4. Temperature of the fire

In those samples with two magnetic components, it has been possible to determine a Component Changing Demagnetization Temperature (CCDT) between the primary and secondary components (Table 5, Fig. 10) which is the maximum demagnetization temperature of the second component. This transition temperature should be equivalent, or at least proportional, to the maximum temperature reached during the second heating. In this way, an approximation of how the heat distribution was like during the fire of 1378 could be determined.

If we considered the values of the samples taken *in situ* in the NW0 hall (P01–13, P01–17, P30–21, P61–08, P61–10 and P73–13), an homogeneous temperature range was observed between 280 and 310 $^{\circ}$ C (Table 5, Fig. 10). This implied that the heat was distributed homogeneously on the floor of this hall, regardless of its distance from walls or proximity to windows, which could have fanned the flames.

Regarding the temperatures measured on the rest of the samples, not collected *in situ*, we observed a great disparity (Table 5, Fig. 10). Two samples (M1–13 and M2–05) would be below the range of 280–310, with 240 °C. Others (M1–21, M2–03 and M23) would fall into the range of 280–310 °C. While above there would be three other ranges: 350–360 °C (M2–04 and M1–24), 440–450 °C (M1–22 and M2–07) and 530–560 °C (M2–09, M2–10 and M2–01).

According to the criteria of the Navarra Fire Service team [34], in the

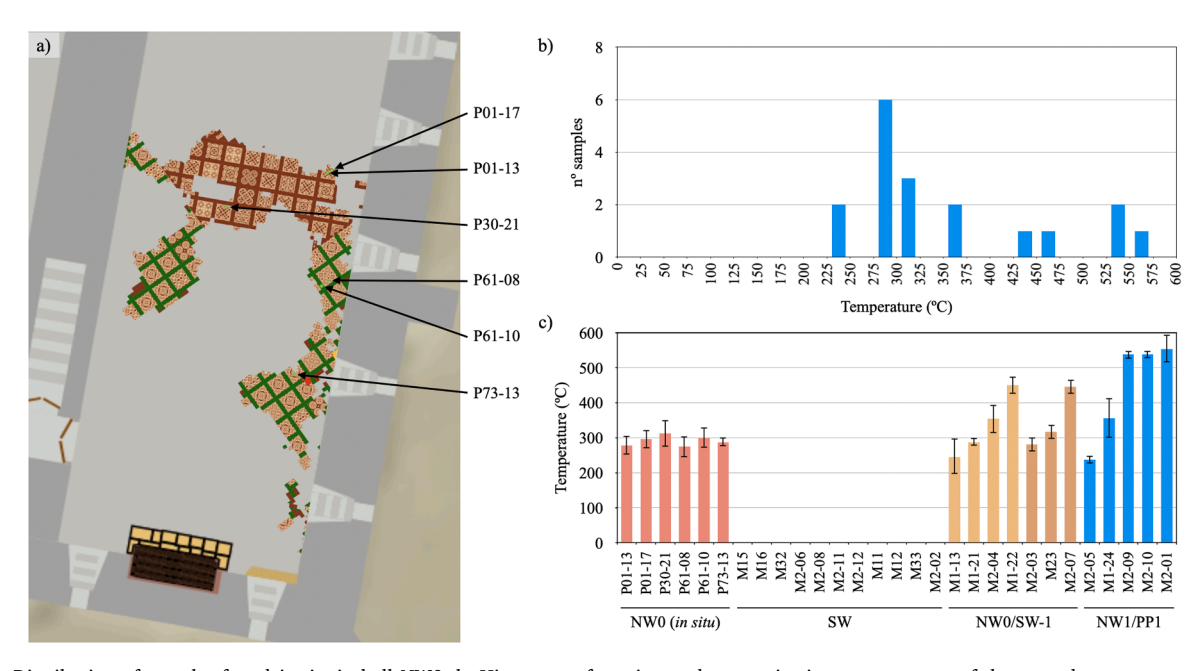


Fig. 10. a: Distribution of samples found in situ in hall NW0. b: Histogram of maximum demagnetization temperatures of the second component. c: Maximum demagnetization temperature of the second component values grouped by pavement and grid.

majority of fires, the heat released by combustion rises to the top of the building with the CO_2 and H_2O generated, raising the temperature of the highest areas of the rooms while creating a negative pressure in the bottom. This negative pressure favours the entry of colder air with a higher concentration of oxygen at the bottom. This phenomenon of convection currents could explain the difference in temperatures between the floor tiles of the NW0 hall and some of those of the first floor (PP1/NW1): M2–09, M2–10 and M2–01.

Another explanation for this variability in temperature ranges may be that some samples were covered by debris, specially those in the ground floor, so were better preserved because they were totally or partially buried by inert materials (tiles, tiles, blocks) that fell from higher floors. These materials would have acted as thermal insulators. On the contrary, the most exposed areas (first floor tiles) would have been more affected by the heat.

4. Conclusions

The integration of materials characterization and magnetic analysis revealed a clear relationship between firing conditions (temperature and atmosphere), mineral composition, colour, and the intensity of Natural Remanent Magnetization (NRM) in ceramic materials. Furthermore, by applying reversely the archaeomagnetic method, this study successfully reconstructed the original orientation of tiles in Tiebas Castle (Spain).

The findings identified at least three distinct tile pavements within the castle, two more than previously known. Details of the newly discovered pavements, such as the arrangement of tiles in two distinct grid patterns and specific decorative motifs, were also uncovered. Additionally, it has been possible to estimate the temperatures reached $(240-540~^{\circ}\text{C})$ during the fire of 1378, providing valuable insights into the thermal impact on the tiles.

These results enhance understanding of the architectural layout of Tiebas Castle before its destruction by fire in 1378 and will help in the virtual reconstruction of its interior. Moreover, this innovative approach demonstrates broader potential for reconstructing historical ceramic structures and their contexts.

CRediT authorship contribution statement

Ruiz-Ardanaz Ivan: Writing – original draft, Visualization, Validation, Software, Methodology, Investigation, Formal analysis, Data curation, Conceptualization. Lasheras Esther: Writing – review & editing, Supervision, Project administration, Methodology, Investigation, Funding acquisition, Conceptualization. Durán Adrián: Writing – review & editing, Supervision, Project administration, Methodology, Investigation, Funding acquisition, Conceptualization.

Declaration of Competing Interest

The authors declare that they have no known competing financial interests of personal relationships that could have appeared to influence the work reported in this paper.

Acknowledgments

The authors thank the Institut de Physique du Globe de Paris (IPGP), the Laboratoire d'Archéologie Moléculaire et Structurale (LAMS) of Sorbonne Université and the Archaeomagnetism Laboratory of the Centro Nacional de Investigación sobre la Evolución Humana (CENIEH) for their collaboration in this study. Particularly grateful for the advice, help in sample preparation, analysis and interpretation of Ágnes Genevey, Yves Gallet, Claudia Álvarez Posada and Josep María Pares. Authors thank Javier Jabat for his advice in fires. The research has the support and financing of the General Directorate of Historical Heritage - Príncipe de Viana of the Government of Navarre under the following projects: "Thibalt. Caracterización arqueométrica de Carreaux de Pavement

procedentes del Castillo de Tiebas (Navarra)" and "Aplicación del arqueomagnetismo y otras técnicas fisicoquímicas para el estudio de la tecnología de fabricación de azulejos medievales navarros", as well as of Ayuntamiento de Tiebas-Muruarte de Reta and the Fundación Sierra de Alaiz. I.R.-A. thanks to the Asociación de Amigos de la Universidad de Navarra for its doctoral scholarship.

Appendix A. Supporting information

Supplementary data associated with this article can be found in the online version at doi:10.1016/j.jeurceramsoc.2025.117344.

References

- [1] R. Thompson, F. Oldfield. Environmental magnetism, Allen and Unwin, 1986 http://doi.org/10.1002/esp.3290130115.
- [2] B.A. Maher, Magnetic properties of modern soils and Quaternary loessic paleosols: paleoclimatic implications, Palaeogeogr. Palaeoclimatol. Palaeoecol. 137 (1998) 25,54
- [3] J.J. Villalaín, La historia del campo magnético terrestre registrada en las rocas: Fundamentos del Paleomagnetismo, Enseñanza de las Ciencias de la Tierra 24 (2016) 261–274. (https://raco.cat/index.php/ECT/article/view/328852).
- [4] N.D. Opdyke, Magnetization processes and magnetic properties of sediments, Int. Geophys. 64 (1996) 26–48, https://doi.org/10.1016/S0074-6142(06)80005-7.
- [5] J.W. Stucki, Properties and behaviour of iron in clay minerals, Dev. Clay Sci. 5 (2013) 559–611, https://doi.org/10.1016/B978-0-08-098258-8.00018-3.
- [6] W. Wu, Z. Wu, T. Yu, C. Jiang, W.S. Kim, Recent progress on magnetic iron oxide nanoparticles: synthesis, surface functional strategies and biomedical applications, Sci. Technol. Adv. Mater. 16 (2015) 023501, https://doi.org/10.1088/1468-6996/ 16/2/023501.
- [7] C.E. Barton, Geomagnetic secular variation: Direction and intensity. Geophysics, Encyclopedia of Earth Science, Springer, Boston, MA, 1989, https://doi.org/ 10.1007/0-387-30752-4-70
- [8] M. Garcés, E. Beamud, La Magnetoestratigrafía y la Escala del Tiempo Geológico basada en las inversiones del campo magnético terrestre, Enseñanza de las Ciencias de la Tierra 24 (2016) 282–293. (https://raco.cat/index.php/ECT/article/view /328854).
- [9] B. Oliva, E.L. Pueyo, Bailes y giros en la corteza superior: de la Tectónica de Placas a la rotación de un pliegue, Enseñanza de las Ciencias de la Tierra 24 (2016) 335–348. (https://raco.cat/index.php/ECT/article/view/328859).
- [10] M. Gómez-Paccard, G. Catanzariti, V.C. Ruiz-Martínez, G. McIntosh, J.I. Núñez, M. L. Osete, A. Chauvin, P. Lanos, D.H. Tarling, D. Bernal-Casasola, J. Thiriot, A catalogue of Spanish archaeomagnetic data, Geophys. J. Int. 166 (2006) 1125–1143, https://doi.org/10.1111/j.1365-246X.2006.03020.x.
- [11] M.C. Brown, G. Hervé, M. Korte, A. Genevey, Global archaeomagnetic data: the state of the art and future challenge, Phys. Earth Planet. Inter. 318 (2021) 106766, https://doi.org/10.1016/j.pepi.2021.106766.
- [12] C. Álvarez, J.M. Parés, D. Granger, M. Duval, R. Sala, I. Toro, New magnetostratigraphic and numerical age of the Fuente Nueva-3 site (Guadix-Baza basin, Spain), Quat. Int. 389 (2015) 224–234, https://doi.org/10.1016/j. quaint.2015.04.0444.
- [13] J.M. Parés, C. Álvarez, M. Sier, D. Moreno, M. Duval, J.D. Woodhead, A.I. Ortega, I. Campaña, J. Rosell, J.M. Bermúdez de Castro, E. Carbonell, Chronology of the cave interior sediments at Gran Dolina archaeological site, Atapuerca (Spain), Quat. Sci. Rev. 186 (2018) 1–16, https://doi.org/10.1016/j.quascirev.2018.02.004.
- [14] C. Álvarez-Posada, J.M. Parés, G. Cuenca-Bescós, J. Van der Made, J. Rosell, J. M. Bermúdez de Castro, E. Carbonell, A post-Jaramillo age for the artefact-bearing layer TD4 (Gran Dolina, Atapuerca): new paleomagnetic evidence, Quat. Geochronol. 45 (2018) 1–8, https://doi.org/10.1016/j.quageo.2018.01.003.
- [15] J.J. Martinena, El Castillo de Tiebas, Zangotzarra 25 (2021) 13–67.
- [16] M. Ramos, Descubrimiento de un pavimento de baldosas decoradas en el castillopalacio de Tiebas, Trabajos de Arqueología Navarra 21 (2009) 317–323.
- [17] M. Diot, Les pavements de Reims et de sa région (Marne), Revue archéologique de Picardie 3-4 (2004) 57-69, https://doi.org/10.3406/pica.2004.2397.
- [18] I. Ruiz-Ardanaz, M. Gil-Fernández, E. Lasheras, A. Durán, Revealing the manufacturing technology to produce the unique carreaux de pavement found in the Iberian Peninsula, Appl. Clay Sci. 231 (2023) 106725, https://doi.org/ 10.1016/j.clay.2022.106725.
- [19] A. Molina-Cardín, S.A. Campuzano, M.L. Osete, M. Rivero-Montero, F.J. Pavón-Carrasco, A. Palencia-Ortas, F. Martín-Hernández, M. Gómez-Paccard, A. Chauvin, S. Guerrero-Suárez, J.C. Pérez-Fuentes, G. McIntosh, G. Catanzariti, J.C. Sastre Blanco, J. Larrazabal, V.M. Fernández Martínez, J.R. Álvarez Sanchís, J. Rodríguez-Hernández, I. Martín Viso, D. Garcia i Rubert, Updated Iberian archeomagnetic catalogue: New full vector paleosecular variation curve for the last three millennia, Geochem. Geophys. Geosystems 19 (2018) 3637–3656, https://doi.org/10.1029/2018GC007781.
- [20] R. Butler, Paleomagnetism: Magnetic Domains to Geologic Terranes, Blackwell Scientific Publications 7 (1992) 121–136. ⟨https://www.geo.arizona.edu/Paleomag/⟩.
- [21] W. Lowrie, Identification of ferromagnetic minerals in a rock by coercivity and unblocking temperature properties, Geophys. Res. Lett. 17 (1990) 159–162.

- [22] J.P. Cogné, PaleoMac: a Macintosh application for treating paleomagnetic data and making plate reconstructions, Geochem. Geophys. Geosystems 4 (1) (2003) 1007, https://doi.org/10.1029/2001GC000227.
- [23] J.D.A. Zijderveld, A. C. Demagnetization of rocks: analysis of results, Dev. Solid Earth Geophys. 3 (2013) 254–286, https://doi.org/10.1016/B978-1-4832-2894-5.50049-5
- [24] A. Khokhlov, G. Hulot, Principal component analysis of paleomagnetic directions: converting a Maximum Angular Deviation (MAD) into an α 95 angle, Geophys. J. Int. 204 (2016) 274–291, https://doi.org/10.1093/gji/ggv451.
- [25] Y.X. Li, K.P. Kodama, Detecting and correcting for paleomagnetic inclination shallowing of sedimentary rocks: a review, Front. Earth Sci. 4 (2016), https://doi. org/10.3389/feart.2016.00007.
- [26] J. Pierce, Y. Zhang, E.B. Hodgin, N.L. Swanson-Hysell, Quantifying inclination shallowing and representing flattening uncertainty in sedimentary paleomagnetic poles, Geochem. Geophys. Geosystems 23 (2022) e2022GC010682, https://doi. org/10.1029/2022GC010682.
- [27] A. Chauvin, Y. Garcia, P. Lanos, F. Laubenheimer, Paleointensity of the geomagnetic field recovered on archaeomagnetic sites from France, Phys. Earth Planet. Int. 120 (2000) 111–136, https://doi.org/10.1016/S0031-9201(00)00148-5

- [28] R.J. Veitch, Calculated anhysteretic susceptibility due to domain wall motion in two-domain magnetite spheres, Geophys. Res. Lett. 11 (1984) 181–184, https:// doi.org/10.1029/GL011i003p00181.
- [29] R.F. King, The remanent magnetism of artificially deposited sediments, Geophys. J. Int. s3 (1955) 115–134.
- [30] I. Ruiz-Ardanaz, E. Lasheras, A. Durán, Mineralogical characterization of carreaux de pavement from northern Spain (Tiebas, Navarre), Minerals 11 (2021) 153.
- [31] A. Pavese, G. Artioli, U. Russo, A. Hoser, Cation partitioning versus temperature in (Mg_{0.70}Fe_{0.23})Al_{1.97}O₄ synthetic spinel by in situ neutron powder diffraction, Phys. Chem. Miner. 26 (1999) 242–250.
- [32] J. López-Sánchez, A. Palencia-Ortas, A. del Campo, G. McIntosh, M. Kovacheva, F. Martín-Hernández, N. Carmona, O. Rodríguez de la Fuente, P. Marín, A. Molina-Cardín, M.L. Osete, Further progress in the study of epsilon iron oxide in archaeological baked clays, Phys. Earth Planet. Int. 307 (2020) 106554, https://doi.org/10.1016/j.pepi.2020.106554.
- [33] I. Ruiz-Ardanaz, E. Lasheras, A. Durán, Applying archaeomagnetic methods to virtually reconstruct the kiln-loading patterns and manufacturing location: Insights from Tiebas Castle (Spain), J. Eur. Ceram. Soc. 45 (10) (2025) 117343.
- [34] (https://www.navarra.es/es/bomberos).